Phase diagram of interfacial growth modes by vapor deposition and its application for ZnO nanostructures

Da-Jun Shu,* Xiang Xiong, Ming Liu, and Mu Wang†

National Laboratory of Solid State Microstructures and Department of Physics, Nanjing University, Nanjing 210093, China
and Collaborative Innovation Center of Advanced Microstructures, Nanjing University, Nanjing 210093, China

(Received 3 May 2017; published 7 September 2017; corrected 12 September 2017)

Interfacial growth from vapor has been extensively studied. However, a straightforward picture of the growth mode under different growth conditions is still lacking. In this paper, we develop a comprehensive interfacial growth theory based on the stochastic approach. Using a critical interisland separation, we construct a general phase diagram of the growth modes. It has been revealed that if the Ehrlich-Schwoebel barrier E_{ES} is smaller than a critical value, the interfacial growth proceeds in a layer-by-layer (LBL) mode at any deposition rate. However, if E_{ES} is larger than the critical value, LBL growth occurs only at very small or very large deposition rates relative to the intralayer hopping rate, and multilayer (ML) growth occurs at a moderate deposition rate. Experiments with zinc oxide growth by chemical vapor deposition have been designed to qualitatively demonstrate the theoretical model. By changing the flux of the carrier gas (nitrogen gas) in chemical vapor deposition, we realize LBL, ML, and then reentrance of LBL homoepitaxial growth of ZnO successively. Moreover, we find that surface kinetics of ZnO is suppressed by decreasing oxygen partial pressure by comparing the experimental observations and theoretical models, which is supported by our recent first-principles calculations. Since the influence of the substrate and the growth species on growth can approximately be represented by binding energy and surface kinetics, we suggest that the phase diagram is essential for interfacial growth of different materials by vapor deposition.

DOI: 10.1103/PhysRevB.96.115411

I. INTRODUCTION

Nucleation and growth on substrate are classic yet still vital topics since understanding the interfacial growth mechanism is essential to control the fabrication of functional materials [1–3]. For far-from-equilibrium growth, the growth modes, and the resulting morphologies are mainly determined by surface kinetics rather than thermodynamics. For example, smooth layer-by-layer (LBL, or two-dimensional) growth is thermodynamically expected for the simplest homoepitaxial growth. However, not only LBL growth but also multilayer (ML, or three-dimensional) growth is observed in vapor growth, depending upon the growth temperature and the deposition rate [4,5]. Nonmonotonic variation of film roughness with temperature has also been reported [6–14]. Extensive study of the interfacial growth kinetics has been carried out in order to understand the growth morphology and hence control the physical properties [15–20]. The interest in interfacial growth has recently been rekindled by designing functional oxide materials, two-dimensional materials, organic semiconductors, and so on [21–23].

Some general theoretical models have been developed for interfacial growth in the past years. For example, by applying rate-equation theory in the nucleation, Tersoff *et al.* predicted that there exists a critical island radius R_c, beyond which a second-layer nucleus forms on top of the island [24]. Depending on whether R_c is smaller or larger than the island separation, the ML or LBL growth mode occurs, which leads to a rough or smooth morphology, respectively. The model has been widely applied for quantitative determination of the interlayer mass transport in epitaxial growth by measuring the fraction of islands on which a stable cluster has nucleated as a function of island size and temperature [25]. In addition to the rate-equation treatment, a stochastic approach, which takes the realistic fluctuations of the adatom population on top of the island into account, has been applied to estimate the nucleation rate [26,27]. The obtained critical island radius R_c shows a different power-law dependence on the growth and kinetics parameters than that from the rate-equation treatment. The stochastic approach is consistent with kinetic Monte Carlo simulations and is expected to be more applicable than the rate equation treatment in dealing with the second-layer nucleation [3,26].

It seems that the framework of the surface growth kinetics has already been established so far. However, in previous work there exist at least two main drawbacks that make a general diagram of growth modes inaccessible. First, almost all previous models merely dealt with certain specific ranges of deposition rate and surface kinetics, which makes the conclusion weak for general situations [24,26,27]. Second, the critical island radius R_c defined in previous studies is actually not an intrinsic quantity because it depends not only upon deposition rate and surface kinetics but also\upon the island-island separation.

In this work we develop a comprehensive growth model based on the stochastic approach, where the formulas have been generalized for application over the whole range of growth conditions. Moreover, a critical interisland separation R_{0c} is introduced, which is completely determined by the deposition rate and the surface kinetics. With these developments we achieve a phase diagram of the growth modes for growth by vapor deposition.

Since the influence of specific substrate and growth species on growth can approximately be represented by binding energy and surface kinetics, the phase diagram is significant for

*djshu@nju.edu.cn
†muwang@nju.edu.cn

interfacial growth by vapor deposition of different materials, including metal, oxides, organic thin films, and so on. To qualitatively verify the theoretical models, we take the vapor growth of ZnO nanorods as an example because of the wide applications of ZnO [28]. We realize LBL, ML, and then the entrance of LBL homoepitaxial growth of ZnO successively by decreasing the deposition rate, as predicted by the phase diagram. Furthermore, combining experimental data with the growth theory, we conclude that the surface kinetics of ZnO is suppressed by decreasing oxygen partial pressure, which is supported by our recent first-principle calculations [29].

II. SECOND-LAYER NUCLEATION

We limit our discussions to the case of a circular monolayer island as an approximation. The first-layer island radius and the island-island separation are denoted as R and R_0, respectively, both in units of the surface cell lattice a_0. Suppose that the growth units are deposited uniformly at a deposition rate F per surface cell a_0^2 in the normal direction. For a certain island separation R_0, both the second-layer nucleation rate Ω and the average number of the second-layer nuclei I increase with the island radius R, which itself grows with time. In order to predict the growth modes, a critical island radius R_c was defined in previous work as that when $I(R_c)$ is unity [24,26,27,30]. In contrast, we propose that a critical island separation R_{0c} is more intrinsic and is key to the description of the interfacial growth.

We define R_{0c} as the average separation between islands that a second-layer nucleus forms atop just when the islands coalesce. In order to obtain R_{0c}, we need to calculate the average nucleus number $\tilde{I}$ on the island at coalescence, i.e., when R grows up to R_0. The nucleation process is described based on the statistical analysis, which was referred to as the lonely adatom model by Krug *et al.* [27]. For simplicity we assume a dimer is a stable nucleus for the time being, which is valid at low temperature. Before the second-layer nucleus forms, a newly deposited atom on the island may either form an isolated adatom with probability P_1 or form a dimer with probability P_2. The isolated adatom later may also form a dimer with a condition probability ω_1 with a subsequently arrived adatom or hops downward to the substrate contributing to the lateral growth of the island. In the steady state $P_2 = P_1\omega_1$, which gives $P_2 = \omega_1/(1+\omega_1)$ since $P_1 + P_2 = 1$. The nucleation rate is thus $\Omega = P_2/\Delta t$, where $\Delta t = 1/F\pi R^2$ is the average time interval between two subsequent deposition events on the island.

The condition probability ω_1 can be approximated as $\omega_1 = h_1 m_1$, where h_1 is the probability that a second adatom is deposited before the first one hops downward to the substrate and m_1 is the encounter probability of the two adatoms. Assuming the island radius R increases with time as $R^2 = FR_0^2 t$, which is reasonable in the steady state, the number of nuclei on the island at island coalescence can be obtained as follows:

$$\tilde{I}(R_0) = \int_0^{R_0} \Omega \frac{dt}{dR} dR = \frac{1}{R_0^2} \int_0^{R_0} \frac{2\pi h_1 m_1 R^3}{1 + h_1 m_1} dR. \quad (1)$$

It is worth noting that in previous studies [27,31] P_2 is assumed to be ω_1, which is valid only when $\omega_1 \ll 1$. For instance, P_2 should be $1/2$ when $\omega_1 = 1$. Therefore the previous approximation cannot cover the whole range of growth conditions.

As shown by Krug *et al.* [27], the two probabilities h_1 and m_1 can be expressed as a function of three time scales. Besides the aforementioned Δt, the other two are the average traversal time required for an adatom to visit all sites of the island, $\tau_{\rm tr} \simeq \pi R^2/\nu$, and the mean residence time of a single adatom τ. In the approximation of the steady state, $\tau = \frac{R^2}{8\nu} + \frac{R}{2\nu'}$, where $\nu = \nu_0 \exp(-E_d)/kT$ and $\nu' = \nu_0 \exp(-E_s)/kT$ are the intralayer and interlayer hopping rates, respectively. The prefactor ν_0 is the attempt frequency, k is the Boltzmann constant, T is the temperature, and E_d and E_s are the corresponding diffusion barriers. In most cases, ν' is smaller than ν due to the presence of the Ehrlich-Schwoebel barrier [16,32,33], $\Delta E_{ES} = E_s - E_d$.

The probability h_1 that a second adatom is deposited on the island during the presence of the first adatom can be obtained by integration

$$h_1 = \int_0^{\infty} \frac{dt}{\Delta t} \exp\left(-\frac{t}{\tau} - \frac{t}{\Delta t}\right) = \frac{\tau}{\tau + \Delta t}. \quad (2)$$

The encounter probability of the two adatoms on the island can be obtained as follows:

$$m_1 = \int_0^{\infty} \frac{dt}{\tau_{tr}} \exp\left(-\frac{2t}{\tau} - \frac{t}{\tau_{tr}}\right) = \frac{\tau}{\tau + 2\tau_{tr}}. \quad (3)$$

Note that if the movements of the two adatoms are independent of each other, the residence time of a pair of adatoms is approximately $\tau/2$. Substituting the expression for Δt, $\tau_{\rm tr}$, and τ into Eqs. (2) and (3), we have

$$h_1 = \frac{1 + \frac{1}{4}\alpha R}{1 + \frac{1}{4}\alpha R + 2\alpha\Gamma/\pi R^3},$$
$$m_1 = \frac{1 + \frac{1}{4}\alpha R}{1 + \frac{1}{4}\alpha R + 4\pi\alpha R}. \quad (4)$$

The deposition rate and surface kinetics are renormalized into two dimensionless parameters α and Γ, which are defined as $\alpha = \nu'/\nu \simeq \exp(-\Delta E_{ES}/kT)$ and $\Gamma = \nu/F$, as adopted in a previous work [26]. Since $\alpha \simeq \exp(-\Delta E_{ES}/kT)$, it is smaller than 1 in the presence of the Ehrlich-Schwoebel barrier.

III. CRITICAL ISLAND SEPARATION

Combining Eq. (1) with Eq. (4), the critical island separation R_{0c} is determined by the condition that $\tilde{I}(R_{0c}) = 1$ for various α and Γ. As shown in Figs. 1(a) and 2(a), R_{0c} increases with α and Γ monotonically. Moreover, it approximately follows a power law, with different exponents in different ranges of α and Γ. In order to analyze the variation of R_{0c} quantitatively, the power-law exponents of R_{0c} with α and Γ are calculated as shown in Figs. 1(b) and 2(b). We find that when $\alpha\Gamma$ is small enough, R_{0c} is independent of Γ. As Γ increases to become large enough, R_{0c} tends to vary as $(\alpha\Gamma)^{1/5}$ for small α. When both α and Γ are large enough, R_{0c} is independent of α and just proportional to $\Gamma^{1/6}$.

Several regions of (α,Γ) can thus be identified according to the power-law exponent of R_{0c}. First, we define region I as the

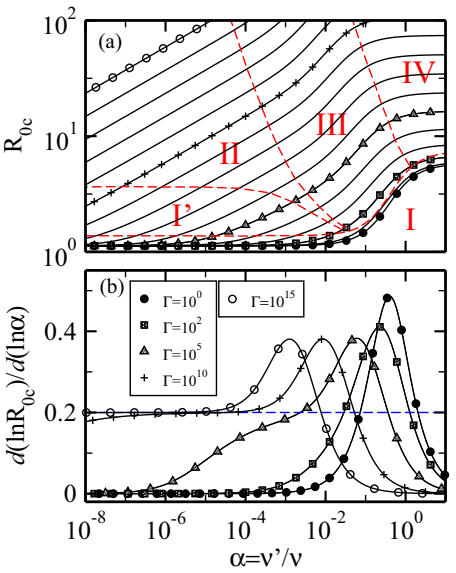

FIG. 1. (a) The logarithmic plot of critical radius R_{0c} as a function of α with different Γ. Γ are from 10^0 (•) to 10^{15} (○), increasing in the uniform exponential index. The four dashed lines are the borders separating five various regions. (b) The logarithmic derivative shows the power-law dependence of R_c on α, i.e., $R_c \sim \alpha^m$. The dashed line indicates the power index of 1/5 in region II.

one where $\alpha\Gamma$ is small enough that $d(\ln R_{0c})/d\ln(\Gamma) < 0.1$. For small α, after the transient region I′, region II is reached when Γ is large enough that $d(\ln R_{0c})/d(\ln\alpha)$ is between 0.19 and 0.21. With increasing α, $d(\ln R_{0c})/d(\ln\alpha)$ first increases and then decreases. After the transient region III,

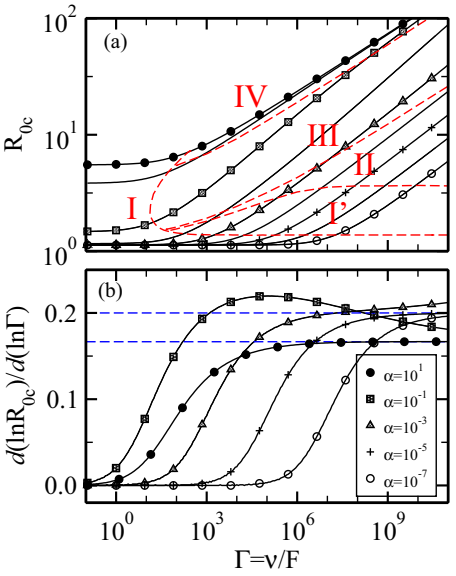

FIG. 2. (a) The logarithmic plot of critical radius R_{0c} as a function of Γ with different α. α are from 10^0 (•) to 10^{-7} (○), increasing in the uniform exponential index. The four red dashed lines are the borders separating five various regions. (b) The logarithmic derivative shows the power-law dependence of R_c on Γ, i.e., $R_c \sim \Gamma^n$. Two blue dashed lines indicate the power index of 1/5 in region II and 1/6 in region IV.

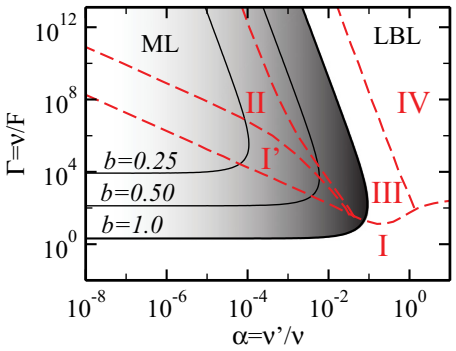

FIG. 3. The phase diagram of the growth modes with variation of α and Γ under the assumption of $i^* = 1$. The solid border curves separating ML growth and LBL growth are determined by $R_{0c} = R_0$ and $R_0 = b\Gamma^{1/6}$. The Roman numerals label the different regions, between which are the dashed border lines.

region IV occurs when both α and Γ are large enough that $d(\ln R_{0c})/d(\ln\alpha) < 0.1$. In this way, the borders between regions are obtained unambiguously, as shown by the red dashed lines in Figs. 1 to 3. It is worth mentioning that R_{0c} varies with α and Γ smoothly. Therefore the exact boundaries can be chosen with some arbitrariness if only the main features of different regions are captured. Different definitions of the boundaries would not influence the main conclusions in this work.

The different dependence of R_{0c} on α and Γ in different regions can be understood as follows. According to Eq. (4), $h_1 \simeq 1$ in region I since $\tau \gg \Delta t$, while $h_1 \simeq \frac{\tau}{\Delta t}$ in regions II, III, and IV since $\tau \ll \Delta t$. Meanwhile, $m_1 \simeq 1$ when $\tau \gg \tau_{\rm tr}$ at the limit of small α (region II and lower part of region I), and $m_1 \simeq 1/16\pi$ since $\tau \ll \tau_{\rm tr}$ at the limit of small α (region IV and upper part of region I). The transient regions I′ and III correspond to the intermediate ranges of Γ and α, respectively. Therefore the expression of R_{0c} in regions I, II, and IV can be analytically obtained according to Eq. (1). It can be summarized as $\tilde{I}(R_0) \simeq (\frac{R_0}{R_{0c}})^n$, where $n = 2$ and R_{0c} increases from $\frac{2}{\sqrt{\pi}}$ gradually to $\sqrt{32}$ in region I, $n = 5$ and $R_{0c} = (\frac{7\alpha\Gamma}{\pi^2})^{1/5}$ in region II, and $n = 6$ and $R_{0c} = 4(\frac{\Gamma}{8\pi})^{1/6}$ in region IV.

Similar to the role of R_c defined in previous work, a ML or LBL growth mode occurs depending on whether R_0 is larger or smaller than R_{0c}. It is worth stressing that R_{0c} is an intrinsic characteristic quantity which is completely determined by α and Γ that contains the information about the deposition rate and the surface kinetics of the island. Different materials and surface orientations possess different surface kinetics, which is included in the two quantities α and Γ. In contrast, the critical island radius R_c defined in previous studies depends additionally upon the interisland separation R_0 [24,26,27,31]. The relation between R_c and R_{0c} is $R_c = (R_0^2 R_{0c}^n)^{1/(n+2)}$. In homoepitaxial growth, $R_0 \propto \Gamma^{1/6}$ according to the standard nucleation theory, where b is a coefficient of order unity [15]. R_c is thus proportional to $\Gamma^{1/12}$, $\Gamma^{4/21}\alpha^{1/7}$, and $\Gamma^{1/6}$ in the limit of small or large α in region I, in region II, and in region IV, respectively. The results are consistent with the Monte Carlo simulations and analytic discussion [26,27].

During ML growth originating from multiple nuclei, the islands failing to coalescence would evolve into separated islands, each growing from a single nucleus. When the single-nucleus growth sets in, R_0 corresponds to the radius of the layer on which the topmost layer forms and decreases as the island grows in the normal direction until it approaches R_{0c}. Therefore R_{0c} also corresponds to the characteristic lateral size of the separated nanostructures [30].

IV. GROWTH MODES

The growth mode can now be predicted by comparing R_0 and R_{0c}. First, we consider the homoepitaxial growth. As shown in Fig. 2, $R_{0c} \sim \Gamma^0$ for small Γ, whereas $R_{0c} \sim \Gamma^{1/5}$ or $\Gamma^{1/6}$ for large Γ, depending on whether α is small or large. Meanwhile, the mean island separation $R_0 \simeq b\Gamma^{1/6}$ according to the classic nucleation theory, where b is a constant in the magnitude of unity [15]. Therefore either two or zero intersection points exist between $R_c(\Gamma)$ and $R_0(\Gamma)$, depending on whether α is small or large. This means that only LBL growth occurs when α is around 1 since R_0 is always smaller than R_c. Instead, ML growth occurs within a moderate range of Γ for small α, in which $R_0 > R_{0c}$ and a second-layer nucleus forms before coalescence.

The phase diagram of the growth mode can thus be constructed as shown in Fig. 3 for three values of b. Evidently, when α is large enough, i.e., when the step-edge barrier is smaller than a critical value, the growth proceeds in the LBL mode at any value of Γ. Otherwise, LBL growth occurs only when Γ is very large or very small, and ML growth occurs within a moderate range of Γ. The range of Γ within which ML growth occurs increases exponentially with increasing the step-edge barrier. Especially, the lower boundary of Γ between LBL and ML growth is in the range of 10^0–10^4. Under the assumption that the attempt frequency ν_0 is 10^{12}/s, the deposition rate F is 0.01 ML/s, and the energy barrier of intralayer diffusion is 0.5 eV, Γ on the order of 10^0 and 10^4 correspond to growth temperatures of 180 and 275 K, respectively, which demonstrates that the theoretical results are realistic in experiments.

The border curve separating the two growth modes is determined by the condition that R_{0c} equals R_0, which gives $\Gamma \sim \alpha^0$ or α^{-6} in the limit of small or large Γ, respectively. For comparison, the borders between the five regions are also shown as red dashed lines, which behaves as $\Gamma \sim \alpha^{-1}$ for the borders between regions I and II (I/I′ and I′/II) and $\Gamma \sim \alpha^{-6}$ for the borders between regions II and IV (II/III and III/IV). In contrast, Rottler and Maass reported that $\Gamma \sim \alpha^{-4/3}$ and $\sim \alpha^{-6}$ for the two border lines, respectively [26]. Morover, according to Fig. 4, the ML and LBL growth modes are always preferred in regions II and IV for $b = 1$, respectively.

In heteroepitaxial growth, the intralayer hopping rate on the substrate is different from that on the island due to the different diffusion barriers. Fortunately, this difference can be conveniently included in the prefactor b. If the diffusion barrier on the substrate is larger than that on the island, the value of b decreases with respect to that in homoepitaxial growth [15], so the α-Γ area for ML growth decreases as shown in Fig. 3.

The assumption that the size of the largest unstable island $i^* = 1$ becomes invalid at higher temperature. Due to the thermal energy, a dimer becomes unstable until it forms a trimer or larger cluster with other adatoms. Suppose $i^* = 2$. In this case, in addition to forming an isolated adatom or a dimer, a newly deposited atom forms a trimer with probability P_3, which satisfies $P_1 + P_2 + P_3 = 1$. In the statistic sense, it satisfies $P_3 = P_2\omega_2$, which leads to $P_3 = \omega_1\omega_2/(1 + \omega_1 + \omega_1\omega_2)$ and then $\Omega = P_3/\Delta t$. Here $\omega_2 = h_2 m_2$ is the condition probability for a dimer to form a trimer with a subsequently arriving adatom. Here $h_2 = \tau'/(\tau' + \Delta t)$ is the probability that an atom is deposited during the presence of an adatom pair, and $m_2 = \tau_d\tau/(\tau_d\tau + \tau_{\rm tr}\tau + \tau_{\rm tr}\tau_d)$ is the probability that the deposited atom encounters a dimer. The two time scales τ' and τ_d are the residence time of the adatom pair and that of a dimer, respectively. Approximately, $\tau' = (\tau_{tr} + \tau_{\rm dis}m_1)\tau/2\tau_{\rm tr}$ and $\tau_d = \tau\tau_{\rm dis}m_1/2\tau_{\rm tr}$, where $\tau_{\rm dis} = \nu_0^{-1}\exp(E_i/kT)$ is the dimer dissociation time and E_i is the binding energy of the dimer [27]. According to the classic nucleation theory [15], the island density for $i^* = 2$ is proportional to $\Gamma^{\frac{1}{2}}\exp(E_i/4kT)$. The island separation is thus $R_0 = b'\Gamma^{\frac{1}{4}}\exp(-E_i/8kT)$, where b' is a prefactor smaller than b. As a demonstration, we set $E_i/E_d = 1$, $\nu_0/F = 10^8$, and $b = 0.25$. The phase diagram for $i^* = 2$ is shown in Fig. 4, constructed in the same way as that for $i^* = 1$. Obviously, the range of ML growth shrinks for a larger critical nucleus size, which is reasonable because the second-layer nucleation is more difficult compared with the case of $i^* = 1$.

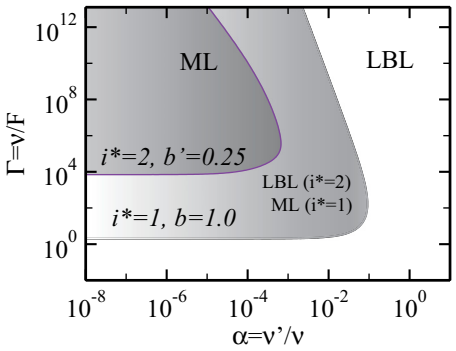

FIG. 4. Schematic comparison of the phase diagram of the growth modes for $i* = 1$ and $i* = 2$, where $i*$ is the number of atoms in the largest unstable island.

In the framework of the phase diagram shown in Figs. 3 and 4, the previously reported influence of the temperature on the film roughness [6–14] can be understood as follows. For simplicity, we first assume that neither the island shape nor the interlayer diffusion mechanism changes with the temperature. According to Fig. 3, if $E_{\rm ES}$ is larger than the critical value, the system will experience a transition from LBL to the ML mode as the temperature decreases and then back to LBL again at still lower temperature. The phase diagram clearly indicates an intrinsic contribution to the previously reported nonmonotonic variation of the surface roughness, although some extrinsic factors may also play important roles [6,7]. More realistically, different diffusion processes may be activated at different T, which inversely influences the island shape and thus the interlayer hopping mechanism and hopping rate [9,34]. Furthermore, adsorption of the residual gas molecule, which itself depends on the temperature,

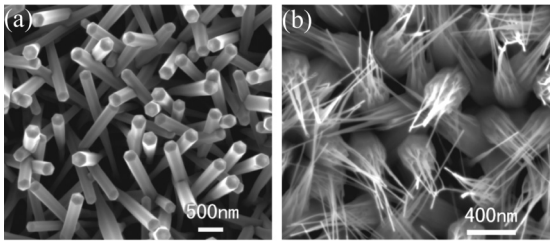

FIG. 5. Typical SEM micrographs of (a) ZnO nanorods obtained in the first growth stage (S1) when the flux of N_2 and O_2 flux is set as 300 and 3 SCCM, respectively, and (b) the ZnO tip grown in the second growth stage (S2) from the residual oxygen gas after cutting off the oxygen flux while the nitrogen flux is kept at 300 SCCM.

changes the surface kinetics properties [25]. Therefore the effective α itself might be nonmonotonically dependent on the temperature, which enhances the nonmonotonic variation of the surface roughness with temperature. If the transition temperature for i^* changing from 1 to 2 is within the crossover region where the growth mode is ML for $i^* = 1$ and LBL for $i^* = 2$, a more complicated temperature dependence of roughness may occur [7].

V. EXPERIMENTS

Because of the complicated influences of temperature on the interfacial growth, we keep temperature unchanged and vary the other parameters to study the growth mechanism in this work. The deposition rate F, for instance, is supposed to influence mainly Γ. In experiments on metal systems, it has been reported that the LBL growth mode changes into the ML growth mode by decreasing or increasing the deposition rate [6,7]. Our phase diagram also suggests that nonmonotonic variation of growth modes can be realized by just changing the deposition rate, independent of the nature of the growth material. Here we study the homoepitaxial growth modes of ZnO nanorods by chemical vapor deposition, controlling the deposition rate by changing the flux of the carrier gas. Despite the fact that the growth of nanostructures of ZnO has been extensively studied [35], its growth kinetics is far from being understood, partly because the oxide surfaces are more complicated than surfaces of simple metals or elemental semiconductors [30,36–38]. We expect that our experiments together with theoretical modeling will provide information about the surface kinetics of zinc oxide.

The ZnO single-crystalline nanorods are synthesized catalyst free in a horizontal tube furnace with zinc powder and O_2. Nitrogen gas is used as the carry gas. The setup of the experiments is similar to that reported in our previous work [30,36,37]. The growth is carried out in two stages. In the first stage (S1), nanorods are grown on the silicon substrate at $T = 600\,^{\circ}\mathrm{C}$, with the O_2 flux set as 3 standard cubic centimeters per minute (SCCM) and N_2 flux set as 300 SCCM. A typical scanning electron microscope (SEM) image of the nanorods grown in S1 is shown in Fig. 5(a). Then the oxygen flux is cut off to trigger the growth from the residual oxygen gas in the second stage (S2) [36,37]; meanwhile, the deposition rate F is modified by changing the N_2 flux to several preset values respectively while keeping the temperature at $600\,^{\circ}\mathrm{C}$.

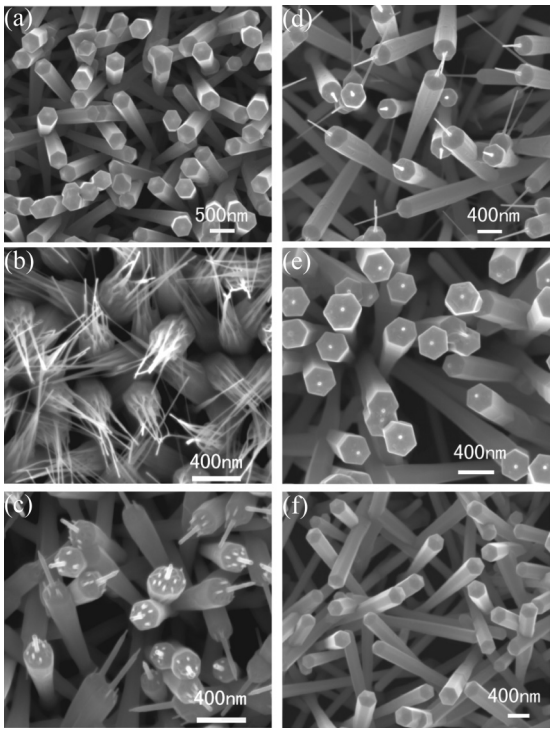

FIG. 6. Typical SEM micrographs of the tip of ZnO nanorods in the second growth stage from the residual oxygen gas, while the nitrogen flux is set as (a) 200, (b) 300, (c) 400, (d) 500, (e) 1500 and (f) 1800 SCCM.

The nanorods obtained in S1 can be regarded as the substrates of the homoepitaxial growth in the very beginning of S2. Therefore according to the change in the morphology from S1 to S2 of the same nanorods, we can obtain information about the homoepitaxial growth modes in the very beginning of S2.

By cutting off the oxygen flux while keeping the nitrogen flux unchanged, one can see that lots of small nanoneedles appear on the tips of the nanorods, as illustrated in Fig. 5(b). X-ray diffraction shows that the needles are ZnO nanorods grown along the c axis [37]. The appearance of multiple needles on each nanorod clearly indicates that in the beginning of S2, ML growth occurs on top of the nanorods grown in S1. By comparing Figs. 5(a) and 5(b), we can see that both the tip radius R_{0c} and the tip separations of the nanorods R_0 decrease when oxygen partial pressure decreases. According to Fig. 2(a), we can conclude that smaller oxygen partial pressure suppresses the interlayer hopping rate ν or the ratio of interlayer hopping rate to the interlayer hopping rate α. This is supported by our recent first-principles calculations of the ZnO (0001) surface [29]. It is worth stressing that the influence of oxygen partial pressure on the morphology of the oxide has been widely reported before [39–41]; however, the underlying mechanisms are not yet clear. Our work clearly shows that the influence of the oxygen partial pressure on the growth morphology is due to the change in surface kinetics.

The tip morphologies grown from the residual oxygen gas in S2 depend sensitively on the nitrogen flux. As the nitrogen flux is increased from 300 SCCM, the density of nanoneedles on top of a single nanorod gradually decreases, as can be seen in Figs. 6(b)–6(e).

When the nitrogen flux is increased to 1800 SCCM or is reduced to 200 SCCM, no needle feature can be identified, as indicated in Figs. 6(f) and 6(a), respectively. This suggests that the initial growth in S2 proceeds in the LBL mode at a sufficiently low or high deposition rate, while the ML growth mode occurs in a moderate range of the deposition rate. This demonstrates that the interfacial growth mode can be experimentally controlled with the guide of the phase diagram. This is an essential step to control the relevant physical properties.

It is worth mentioning that the needlelike morphology obtained in ML growth of ZnO is different from the wedding-cake morphology of metal island growth [25,27]. The difference may partly be due to the fact that the ZnO(0001) surface is a polar surface, which may induce shield effects during the deposition process [30,42]. Whatever the underlying mechanism is for this difference, it should not influence the identification of the ML growth mode at the beginning of the second growth stage.

The decreasing density of needles on the top from Figs. 6(b) to 6(e) shows that when nitrogen flux increases (deposition rate F decreases), the nucleation rate decreases gradually, and then LBL growth takes place. In contrast, at low nitrogen flux (large F), LBL growth is mediated by easier coalescence of the nuclei due to the increasing nucleus density. The experiments are consistent with what is expected from our phase diagram. Since $\Gamma = \nu/F$, the LBL growth at high and low temperatures follows a mechanism similar to that for low F and high F, respectively.

VI. CONCLUSION

In summary, by defining an intrinsic critical interisland separation, a general phase diagram of growth modes for vapor growth has been provided that covers a wide range of growth conditions. Vapor growth of zinc oxide nanorods has been used to qualitatively verify the growth theory. By increasing the flux of the carrier gas, we realized LBL, ML, and then reentrance of LBL growth successively, as predicted by the phase diagram. Moreover, a combination of the experimental data and the theory indicates that the surface kinetics of ZnO is suppressed by decreasing oxygen partial pressure, which is supported by our recent simulations. We believe the phase diagram of growth modes in vapor deposition growth applies for many different materials and can be helpful in understanding and controlling the growth process.

ACKNOWLEDGMENTS

This work was supported by the National Natural Science Foundation of China (Grants No. 11174123, No. 11474157, No. 11674155, No. 11634005, and No. 11574141), the Basic Research Project of Jiangsu Province (Grants No. BK20161390 and No. BK20160065), and the Ministry of Science and Technology of China (Grant No. 2017YFA0303702).

[1] I. V. Markov, *Crystal Growth for Beginners*, 2nd ed. (World Scientific, Singapore, 2003).
[2] A. A. Virkar, S. Mannsfeld, Z. Bao, and N. Stingelin, Adv. Mater. **22**, 3857 (2010).
[3] M. Einax, W. Dieterich, and P. Maass, Rev. Mod. Phys. **85**, 921 (2013).
[4] Z. Zhang and M. G. Lagally, *Morphological Organization in Epitaxial Growth and Removal* (World Scientific, Singapore, 1996).
[5] Z. Y. Zhang and M. G. Lagally, Science **276**, 377 (1997).
[6] R. Kunkel, B. Poelsema, L. K. Verheij, and G. Comsa, Phys. Rev. Lett. **65**, 733 (1990).
[7] F. Tsui, J. Wellman, C. Uher, and R. Clarke, Phys. Rev. Lett. **76**, 3164 (1996).
[8] J. Jacobsen, K. W. Jacobsen, P. Stoltze, and J. K. Norskov, Phys. Rev. Lett. **74**, 2295 (1995).
[9] C. R. Stoldt, K. J. Caspersen, M. C. Bartelt, C. J. Jenks, J. W. Evans, and P. A. Thiel, Phys. Rev. Lett. **85**, 800 (2000).
[10] W. C. Elliott, P. F. Miceli, T. Tse, and P. W. Stephens, Phys. Rev. B **54**, 17938 (1996).
[11] H. J. Ernst, F. Fabre, R. Folkerts, and J. Lapujoulade, Phys. Rev. Lett. **72**, 112 (1994).
[12] W. F. Egelhoff and I. Jacob, Phys. Rev. Lett. **62**, 921 (1989).
[13] P. Smilauer, M. R. Wilby, and D. D. Vvedensky, Phys. Rev. B **47**, 4119 (1993).
[14] Y. Shim and J. G. Amar, Phys. Rev. B **81**, 045416 (2010).
[15] J. A. Venables, G. D. T. Spiller, and M. Hanbucken, Rep. Prog. Phys. **47**, 399 (1984).
[16] P. Politi, G. Grenet, A. Marty, A. Ponchet, and J. Villain, Phys. Rep. **324**, 271 (2000).
[17] A. Ohtomo, D. A. Muller, J. L. Grazul, and H. Y. Hwang, Nature (London) **419**, 378 (2002).
[18] G. Logvenov, A. Gozar, and I. Bozovic, Science **326**, 699 (2009).
[19] A. Ohtomo and H. Y. Hwang, Nature (London) **427**, 423 (2004).
[20] A. Tsukazaki, Science **315**, 1388 (2007).
[21] J. W. Reiner, F. J. Walker, and C. H. Ahn, Science **323**, 1018 (2009).
[22] J. Mannhart and D. G. Schlom, Science **327**, 1607 (2010).
[23] H. Klauk, Chem. Soc. Rev. **39**, 2643 (2010).
[24] J. Tersoff, A. W. Denier van der Gon, and R. M. Tromp, Phys. Rev. Lett. **72**, 266 (1994).
[25] M. Kalff, G. Comsa, and T. Michely, Phys. Rev. Lett. **81**, 1255 (1998).
[26] J. Rottler and P. Maass, Phys. Rev. Lett. **83**, 3490 (1999).
[27] J. Krug, P. Politi, and T. Michely, Phys. Rev. B **61**, 14037 (2000).
[28] A. Kolodziejczak-Radzimska and T. Jesionowski, Materials **7**, 2833 (2014).
[29] Q.-Y. Ruan, J.-C. Ye, D.-J. Shu, and M. Wang, Phys. Rev. B **96**, 115412 (2017).
[30] D.-J. Shu, X. Xiong, Z.-W. Wang, Z. Zhang, M. Wang, and N.-B. Ming, J. Phys. Chem. C **115**, 31 (2011).
[31] J. Krug, J. Stat. Phys. **87**, 505 (1997).
[32] G. Ehrlich and F. G. Hudda, J. Chem. Phys. **44**, 1039 (1966).

[33] R. L. Schwoebel and E. J. Shipsey, J. Appl. Phys. **37**, 3682 (1966).
[34] H. Roder, K. Bromann, H. Brune, and K. Kern, Phys. Rev. Lett. **74**, 3217 (1995).
[35] Z. L. Wang, Mater. Today **7**, 26 (2004).
[36] M. Liu, G.-B. Ma, X. Xiong, Z.-W. Wang, R.-W. Peng, J.-G. Zheng, D.-J. Shu, Z. Zhang, and M. Wang, Phys. Rev. B **87**, 085306 (2013).
[37] M. Liu, C. Meng, Z.-H. Xue, X. Xiong, D.-J. Shu, R.-W. Peng, Q. Wu, Z. Hu, and M. Wang, Europhys. Lett. **104**, 18004 (2013).
[38] M. Valtiner, M. Todorova, G. Grundmeier, and J. Neugebauer, Phys. Rev. Lett. **103**, 065502 (2009).
[39] H. Kato, M. Sano, K. Miyamoto, and T. Yao, Jpn. J. Appl. Phys. **42**, L1002 (2003).
[40] H. Kato, M. Sano, K. Miyamoto, and T. Yao, Jpn. J. Appl. Phys. **42**, 2241 (2003).
[41] H. Xu, K. Ohtani, M. Yamao, and H. Ohno, Appl. Phys. Lett. **89**, 071918 (2006).
[42] D.-J. Shu, X. Xiong, Z.-W. Wang, M. Wang, R.-W. Peng, and N.-B. Ming, arXiv:1003.2265.